

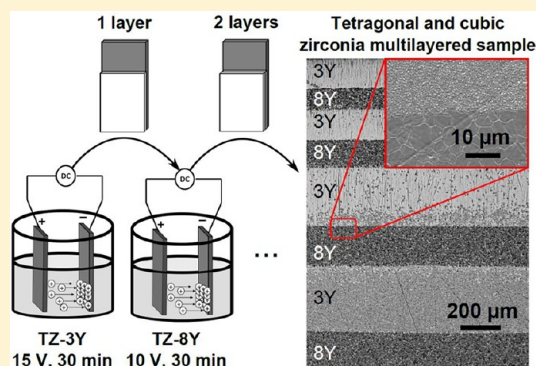
Tetragonal and Cubic Zirconia Multilayered Ceramic Constructs Created by EPD

Carolina Mochales,^{*,†} Stefan Frank,[†] Rolf Zehbe,[‡] Tania Traykova,[‡] Christine Fleckenstein,[†] Anke Maerten,[‡] Claudia Fleck,[‡] and Wolf-Dieter Mueller[†]

[†]Dental School, "Charité" Universitaetsmedizin Berlin, 14197 Berlin, Germany

[‡]Materials Engineering, Berlin Institute of Technology, 10623 Berlin, Germany

ABSTRACT: The interest in electrophoretic deposition (EPD) for nanomaterials and ceramics production has widely increased due to the versatility of this technique to effectively combine different materials in unique shapes and structures. We successfully established an EPD layering process with submicrometer sized powders of Y-TZP with different mol percentages of yttrium oxide (3 and 8%) and produced multilayers of alternating tetragonal and cubic phases with a clearly defined interface. The rationale behind the design of these multilayer constructs was to optimize the properties of the final ceramic by combining the high mechanical toughness of the tetragonal phase of zirconia together with the high ionic conductivity of its cubic phase. In this work, a preliminary study of the mechanical properties of these constructs proved the good mechanical integrity of the multilayered constructs obtained as well as crack deflection in the interface between tetragonal and cubic zirconia layers.



INTRODUCTION

Zirconia (ZrO_2) ceramics exhibit excellent corrosion resistance and high-temperature ionic conductivity, which makes them promising materials for applications operating in aggressive environments, for cutting tools, or as solid electrolytes in fuel cells and in oxygen sensors. Moreover, they exhibit a good chemical and structural stability, mechanical strength, and toughness, coupled to a Young's modulus on the same order of magnitude as stainless-steel alloys. All this makes them a very versatile ceramic material. Furthermore, the excellent biocompatibility and bioinertness coupled to good mechanical properties makes them suitable as biomaterial for dental and orthopedic applications.^{1,2}

Zirconia occurs in three crystal modifications at low-pressure conditions: monoclinic, tetragonal, and cubic. The monoclinic phase is stable up to 1170 °C, whereas the tetragonal phase is stable between 1170 and 2370 °C, and the cubic one is stable above 2370 °C.¹

Doping of zirconia results in stabilization of the tetragonal phase at lower dopant concentrations (below ~8 mol %) and in stabilization of the cubic phase at higher ones (above ~8 mol %). Common dopants are CaO, MgO, CeO_2 , and Y_2O_3 . The stabilization of the tetragonal or the cubic phases at room temperature results in a remarkable increase in mechanical toughness (tetragonal form) or ionic conductivity (cubic form) to values significantly higher than those for other ceramics.^{1,3} This high ionic conductivity of the cubic zirconia makes it a very suitable material as electrolyte for solid oxide fuel cells (SOFCs). Tetragonal zirconia polycrystals (TZPs) are being used in the dental and orthopedic field due to their relatively

high toughness, which is due to a phenomenon generally referred to as transformation toughening. Tensile stresses induce transformation of the metastable tetragonal (t) phase to the stable monoclinic (m) phase, resulting in a volume increase of about 3 to 5% and corresponding compressive residual stresses, which impede crack propagation by closing and shielding the crack from the external load.^{4–6} Moreover, the stabilizer (i.e., yttria) interruption of the crystal lattice increases the thermal insulation capacity of zirconia ceramics. In this direction, the use of yttria-stabilized ceramics as thermal barrier coatings (TBCs) is of big importance.⁷

Because of its wide range of applications, zirconia coatings and the methodology to obtain them are being subject of many research works.^{8,9} Several coating techniques have been proposed and studied, such as vapor deposition,¹⁰ plasma spraying,¹¹ sol-gel,¹² and casting techniques¹³ among others. Another promising method to produce ceramic coatings and, more generally, hierarchically structured ceramic composites is electrophoretic deposition (EPD).^{14,15} The interest in EPD of ceramics or ceramic composites lately increased due to its versatility regarding the achievable microstructures, the flexibility regarding the achievable shape, and the easy processing.^{16–18}

Special Issue: Electrophoretic Deposition

Received: June 29, 2012

Revised: November 5, 2012

Published: November 6, 2012



Apart from different ZrO_2 -based composites and different structural designs, a promising approach to enhance and optimize engineering properties for zirconia-based ceramics has been found in hierarchically structuring of zirconia with different amounts of doping.^{19–21} Indeed, the stabilization of zirconia to its tetragonal or cubic phase by just changing the amount of doping provides the possibility to try to combine the properties of these two different phases and improve the final response of the ceramic structure to fulfill the specific requirements of each application.

We therefore established the layered deposition of alternating zirconia materials with different concentrations of yttria dopant (3 and 8 mol %) via EPD with the underlying goal to produce zirconia ceramic constructs combining the good mechanical toughness of tetragonal zirconia and the good ionic conductivity of cubic zirconia. In a first step, process parameter windows were investigated as to establish reproducible and reliable production routines of layered specimens in a size suitable for rudimentary mechanical testing. The microstructure of the layers and the interfaces of the constructs we made were analyzed by SEM and EDX to gain information on the grain size, the interfacial bonding, and the yttria doping distribution. To investigate whether the chosen designs are promising to increase the toughness of cubic zirconia, we performed microindentation tests, and the resulting crack paths were evaluated.

MATERIALS AND METHODS

Multilayered specimens of alternating tetragonal and cubic stabilized zirconia were produced by EPD. Two different Y_2O_3 -stabilized ZrO_2 powders (TZ-3Y with 3 mol % Y_2O_3 and TZ-8Y with 8 mol % Y_2O_3) from Tosoh (Shunan, Japan) were used for the experimental investigations. According to the data given by the manufacturer, the used powder batches (Z309826P, TZ-3Y and Z809838P, TZ-8Y) contained 5.22 wt % Y_2O_3 for TZ-3Y and 13.60 wt % Y_2O_3 for TZ-8Y. The specific surface areas and crystallite sizes were 14.8 m^2/g and 26 nm for TZ-3Y and 13.5 m^2/g and 23 nm for TZ-8Y. To characterize the used reactants in more detail, the phase composition of the as-received zirconia powders was analyzed by means of powder X-ray diffraction (PXRD; Bruker D8 Advance diffractometer, Karlsruhe, Germany). The PXRD measurements were performed in reflectance Bragg–Brentano geometry using $\text{Cu K}\alpha 1$ radiation with a curved Germanium 111 primary monochromator operated at 40 kV accelerating voltage and 40 mA current. Data were acquired from 15 to 90° 2θ scan using a step size of 0.025° and step time of 2 s. The peaks were matched with JCPDS files nos. 42-1164, 49-1642, and 37-1484 for the tetragonal, cubic, and monoclinic phases, respectively.

Suspensions consisting of 200 ml of ethanol (96% ethanol, Merck, Darmstadt, Germany) with 40 wt % powder were prepared. Acetic acid (Carl Roth, Karlsruhe, Germany) was added to adjust the pH of the solution. The conductivity and the pH of the suspensions were measured with a redox meter PCE-PHD 1 (PCE Inst., Meschede, Germany). The pH was set to 6.35 and 5.78 for the TZ-3Y and TZ-8Y suspensions, respectively, and the respective conductivity values were 48.5 (TZ-3Y) and 211 μS (TZ-8Y).

Prior to use, the suspensions were magnetically stirred for at least 3 days, followed by ultrasonication for at least 3 min by means of an ultrasonic horn (Kontes micro ultrasonic cell disruptor, Scientific Glassware/Instruments, Vineland, NJ).

Aluminum electrodes were used with a relative distance of 2.5 cm. The deposition area was around 25–30 mm by 10 mm. The EPD process was carried out at a constant DC voltage of 15 V for the TZ-3Y layers and of 10 V for the TZ-8Y layers. TZ-3Y and TZ-8Y layers were deposited consecutively with a fixed deposition time of 30 min for each layer (Figure 1).

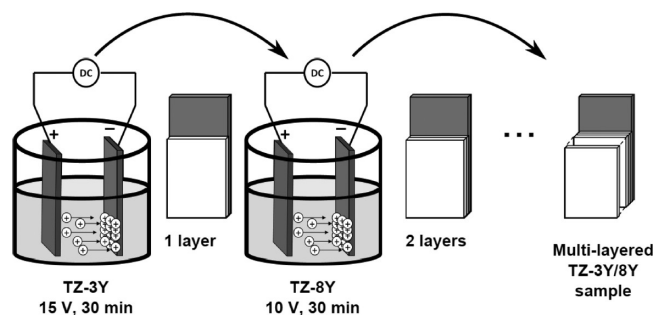


Figure 1. Scheme of the EPD process used to obtain the tetragonal and cubic multilayered specimens.

Single-layer samples were also deposited for both the TZ-3Y and TZ-8Y powders with a deposition time of 1 h to record XRD patterns and analyze the crystallographic phases present after sintering.

After drying and removal from the electrode, the deposited multilayered and single-layer specimens were sintered at 1450 °C for 3 h in a VITA Zyrcomat oven (Vita Zahnfabrik, Bad Saeckingen, Germany). To achieve a smooth surface to perform μ -indentation, the multilayered samples were ground and polished down to a grain size of 1 μm using polishing cloths and diamond suspensions. To reverse the t-m transformation due to the mechanical manipulation, we annealed these samples again at the sintering temperature (1450 °C) for another 3 h.

The obtained zirconia multilayered specimens were investigated via optical microscopy (Zeiss Axiophot, Carl Zeiss, Jena, Germany), atomic force microscopy (nanosurf easyscan 2, nanosurf, Langen, Germany), Raman microscopy (LabRAM HR, Horiba Jobin Yvon, HORIBA Europe, Germany), and scanning electron microscopy (SEM; FEI Quanta 600 FEG, FEI, Eindhoven, The Netherlands). Layer thicknesses were measured from the obtained optical images with DHS software (Dietermann & Heuser Solution, Greifensee-Beilstein, Germany). The microstructure of the two different layers (cubic and tetragonal) and specifically the interface between them was analyzed using electron microscopy. The grain size of the tetragonal grains present in the TZ-3Y layers and the cubic grains in the TZ-8Y layers was analyzed according to DIN EN ISO 643 as the mean grain area from which a mean grain diameter was calculated. In addition to this ISO specification, the mean feretMax- and the mean feretMin-diameters were analyzed as well. All analyses were performed using ImageJ²² on binarized images following image processing steps as described elsewhere.²³

To evaluate the yttria-distribution over the interface, energy dispersive X-ray (EDX) analysis was performed with an SEM S-2700 (High-Technologies, Japan) equipped with an EDX system (remX, Bruchsal, Germany) with a Si(Li) detector and a Moxtek AP 1.3 window (active area 10 mm^2). The EDX-measurements were performed at 20 kV and a working distance between the detector and the sample of 17 mm. Two linescans were recorded to measure the yttrium content along the interfaces with two different magnifications. A first overview of

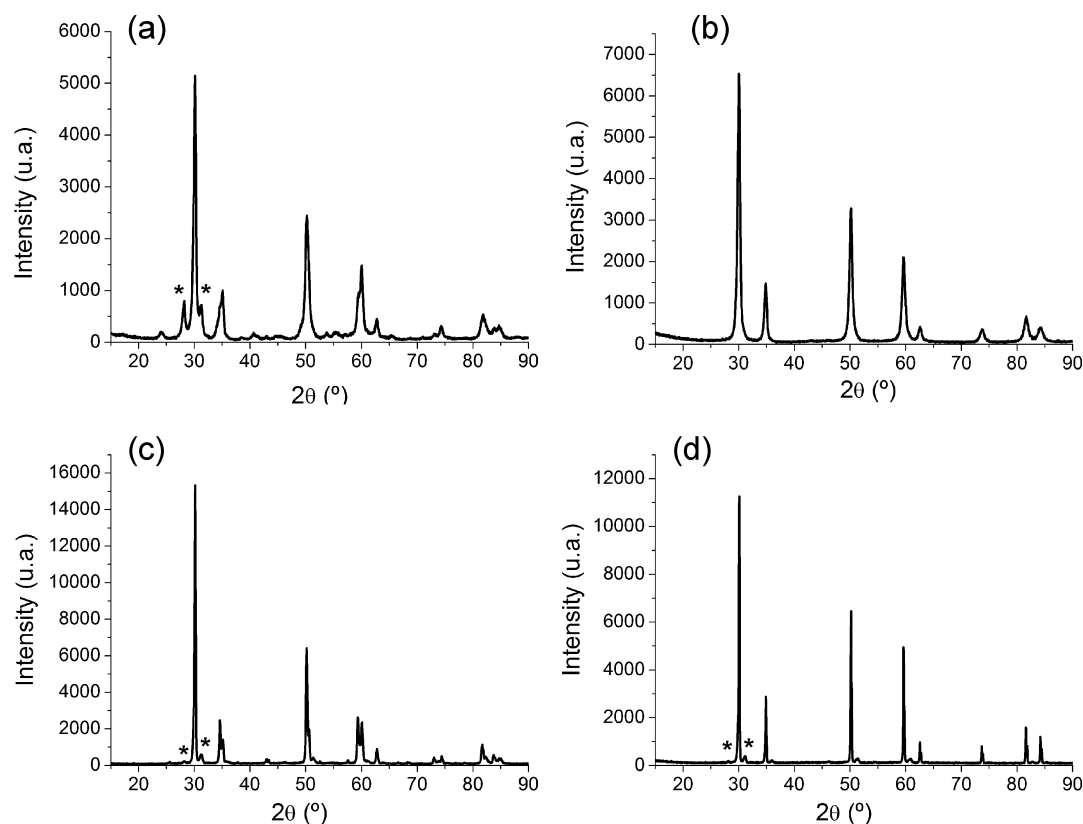


Figure 2. XRD of (a) TZ-3Y and (b) TZ-8Y raw powders used in this work and (c) TZ-3Y and (d) TZ-8Y EPD obtained layers. (*) Main monoclinic peaks.

the zirconia layers was performed along a line of 2000 μm length with a step size of 5 μm and a measuring time per step of 10 s. A second linescan that was part of the first line was recorded with a length of 20 μm with a smaller step size of 0.05 μm (measuring time per step also 10 s) to measure the local yttrium distribution orthogonal to the interface between the TZ-3Y and the TZ-8Y layers with higher precision. Data were evaluated with the software IDFix (remX). Simulation of the EDX line scan intensity along the border of a simulated grain boundary of TZ-3Y and TZ-8Y grains was performed using Casino²⁴ with the program standard physical model. An EDX line scan was simulated for 20 keV, 10 nm beam radius, 100 000 electrons, and a specimen tilt of 15 $^{\circ}$ scanning a length of 4 μm in steps of 100 nm. For the TZ-3Y and TZ-8Y grains, an atomic composition was defined corresponding to results from the real EDX-measurements.

To study the crack formation and growth within the layers and how they are influenced by the interfaces, we introduced Vickers microindents (Zwick 3212, Zwick, Ulm, Germany) into the polished surfaces. They were prepared by application of a 5 kg load (49 N) for a duration of 12 s. The crack propagation for an angle of incidence of 45 $^{\circ}$ was studied starting from the TZ-3Y or the TZ-8Y layer. The InfiniteFocus G4Microscope (IFM) (Alicona Imaging, Grambach/Graz, Austria) was used to observe the indented surfaces. Further investigations of the topography were performed using the nanosurf easyscan 2 AFM. This methodology was chosen as the transformation toughening mechanism for zirconia, and the resulting change from the tetragonal to the monoclinic phase induces a volume increase that should be detectable as a height increase in topography. This mechanism was further cross validated using

Raman microscopy to specifically detect the crystallographic phases and their local variation. Excitation was performed at a wavelength of 514 nm with a laser energy of 5 mW at room temperature. A total of eight spot measurements were done for a wavenumber range between 150 and 700 cm^{-1} . The characteristic Raman shifts for tetragonal, monoclinic, and cubic zirconia were compared with the values given in the work by Phillippi et al.²⁵ Indicative shifts were specifically marked at ~180 (monoclinic), at ~625 (cubic) and at ~640 cm^{-1} (tetragonal).

To characterize the potential for possible crack bifurcation, we evaluated the orientation changes of cracks propagating through the layers' interface using the IFM software on Alicona interferometry optical images taken at 50 \times and 100 \times magnifications. Moreover, the fractured surface of a multi-layered specimen subjected to four-point bending test (4-PBT) was observed by SEM.

RESULTS

PXRD of the raw zirconia powders showed a main tetragonal phase with a small amount of the monoclinic low temperature phase for the TZ-3Y raw powder (Figure 2a) and a single cubic phase for the TZ-8Y (Figure 2b). The EPD-deposited single TZ-3Y layer after sintering also showed a main tetragonal phase with a small amount of the monoclinic low temperature phase as for the raw powder layer (Figure 2c). For the EPD-deposited single TZ-8Y layer after sintering a main cubic phase was detected in accordance with the starting raw powder (Figure 2d). However, it must be noticed that also a small amount of monoclinic phase was detected after sintering the TZ-8Y deposited layer (Figure 2d).

Figure 3a shows one of the several obtained zirconia multilayered specimens. The used EPD process with constant

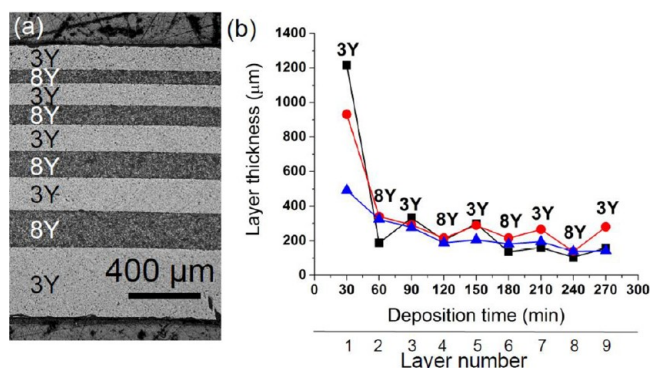


Figure 3. Overview of a multilayered specimen obtained by EPD (a) and evolution of the EPD layers thickness with the whole deposition time (b).

deposition times for each layer resulted in several multilayered specimens with layers of different thicknesses between 1216 and 142 μm for the TZ-3Y and between 383 and 139 μm for the TZ-8Y. Figure 3b shows the evolution of the layers thickness for three sample replicates (with nine layers each) obtained from the same starting suspensions. Thus, one TZ-3Y and one TZ-8Y suspension were prepared and used to produce consecutive multilayered samples of nine layers each, starting and ending with a TZ-3Y layer. The first TZ-3Y layer

experiences a significant decrease when comparing between the three different replicates obtained. The next TZ-8Y layer is significantly thinner than the previous TZ-3Y layer for the three replicates, especially for the first one (black). The following TZ-3Y layers decrease with an exponential tendency with the deposition time (understanding it as the deposition time during the whole EPD process to obtain the investigated sample) or “order” of deposition of the layers. In the case of the TZ-8Y, the decreasing tendency is not so clear for the first and second replicates, although it is shown in the third replicate.

The result of the grain size analysis performed in two areas of one TZ-3Y and one TZ-8Y layer near their interface is displayed as a histogram in Figure 4d,e. The mean results are presented in Table 1.

The EDX-linescan clearly confirms the layered structure of the alternating TZ-3Y and TZ-8Y layers. Although the backscattered electron image (Figure 5a) shows only a weak contrast, the EDX-linescan well corresponds to these data (Figure 5b), not only for the yttrium $L\alpha$ -signal but similarly for the zirconium $L\alpha$ - and the oxygen $K\alpha$ -signals. Scanning across the phase boundary at a higher resolution indicates a yttrium-gradient across the interface. This, however, is apparently not linked to a diffusion zone but to the size of the interaction volume of the electron beam with the material. This can clearly be seen for the simulated EDX-spectrum, which shows the same slope over the interface of the two neighboring phases even though they were assumed to have no yttrium gradient.

Figure 6 shows an optical micrograph of an indent in the tetragonal TZ-3Y next to the cubic TZ-8Y layer. The distance

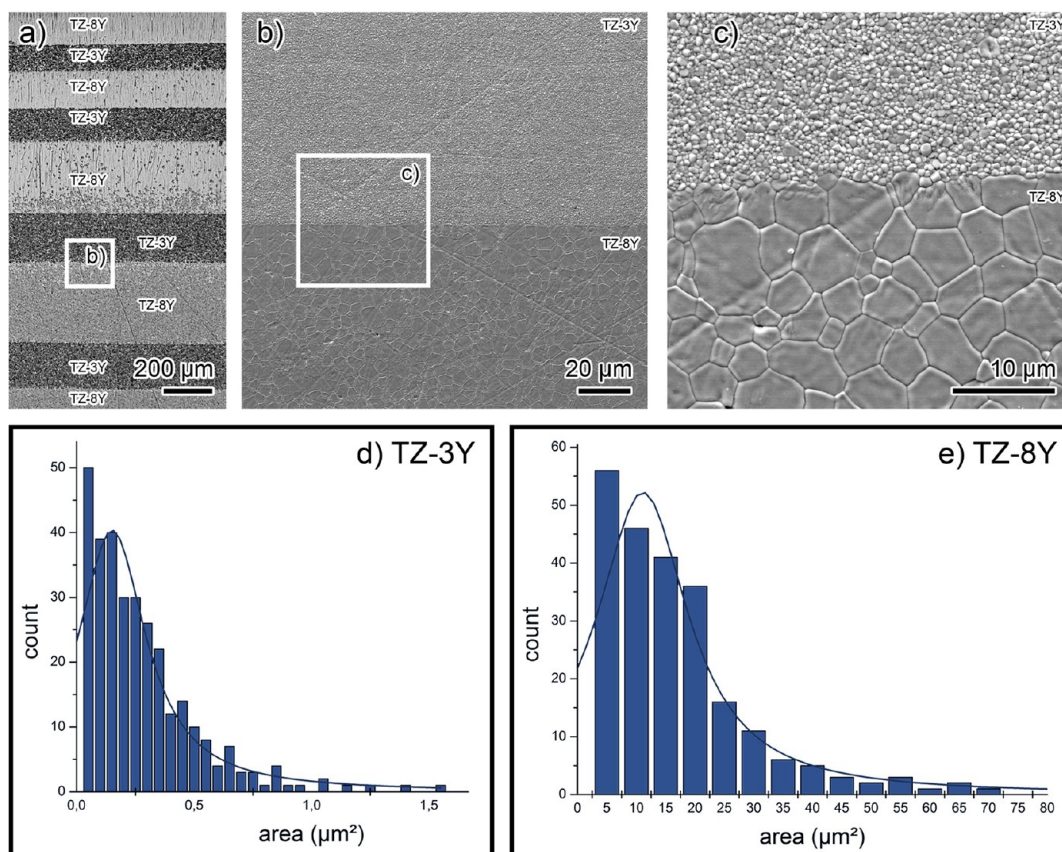
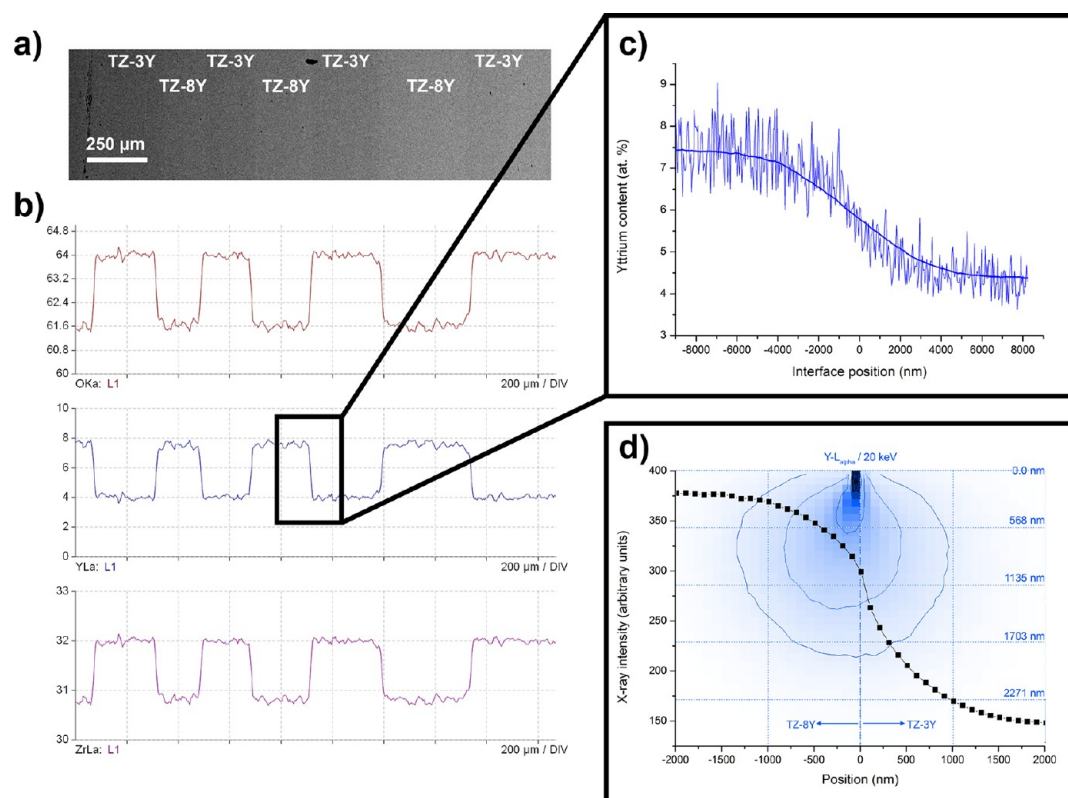


Figure 4. SEM images of TZ-3Y and TZ-8Y (a) overview of multilayer and (b) magnification of layer interface (1500 \times), (c) magnification at 6000 \times , and (d,e) corresponding grain size histograms.

Table 1. Grain Size Analysis for the Tetragonal and Cubic Grains in the TZ-Multilayer (Grain Area and Grain Diameter Are Calculated According EN ISO 643)^a

	grain area (\bar{O} , μm^2)	grain diameter (\bar{O} , μm)	Ferret diameter (\bar{O} , μm)	
			max	min
TZ-3Y (tetragonal) ^b	0.30 ± 0.99	0.55 ± 1.00	0.78 ± 0.91	0.47 ± 0.57
TZ-8Y (cubic) ^c	14.32 ± 12.68	3.78 ± 3.56	5.57 ± 3.27	3.48 ± 1.75

^aAll values are given \pm SD. ^b $n = 229$. ^c $n = 312$.**Figure 5.** BSE image of multilayer structure (a) and EDX line scan across multilayer with EDX measurements for Zr, Y, and O (b). Magnification for line scan across layer interface (c) and Monte Carlo simulation of an EDX line scan with electron-solid interaction and corresponding penetration depth (d).

from the center of the indents to the interface is $\sim 40 \mu\text{m}$. Superimposed on this image is the AFM image showing the color-coded topography. This is additionally visualized in Figure 6b in a pseudo-3D-representation. Figure 6a further shows the Raman spectra measured in the spots indicated by the individual numbers. The peaks in these spectra that are characteristic for the interesting crystallographic phases have been color-coded: blue, red, and green denote the peaks for the monoclinic, tetragonal, and cubic phases, respectively. The measurements indicate a mostly tetragonal composition at points "1", "6", and "7", the existence of tetragonal and monoclinic phases at points "3", "4", "5", and "8", and only cubic phase at point "2". As expected, a topographic height increase indicating a volume increase is linked to the existence of monoclinic phase fractions. It may therefore safely be assumed that in these areas phase transformation from tetragonal to monoclinic took place due to the stresses during indentation. Vickers indents within one layer and near the interface of a second layer with different composition were introduced to analyze the influence of the interface and a second phase with lower toughness on the crack propagation and to evaluate possible crack stopping, bifurcation, or

deflection mechanisms due to this interface and the change in properties. If the 3Y-layer was indented near the interface to an 8Y-layer, then the cracks passed through the interface (Figure 6c), showing a deflection with an angle variation of $\sim 10^\circ$. For instance, the crack on the left, lower corner of the indent shown in Figure 6 showed an angle of incidence relative to the interface of $\sim 32^\circ$ and an angle of refraction of $\sim 43^\circ$. Furthermore, the initial crack was not only deflected but also stopped on the surface. A second, subsequent crack is seen on the surface (red arrows), which may be due to the crack deflection under the surface. Moreover, unexpectedly, these cracks emanating from an indent in the 3Y-layer and running toward the 3Y–8Y interface did not go through the indent corners but seem to reach the surface on the edge of the indent a little away from the corner. From these surface images, it is difficult to state if the origin of the cracks was the tip of the indent or not. A different behavior is seen for the crack emanating from the right corner (Figure 6d) of the indent (red circle). Contrary to the other two cracks deflecting through the 3Y–8Y interface, this crack did not pass through the interface but stopped before reaching it. On the side of the indent away from the interface, the cracks (upper cracks seen in Figure 6a)

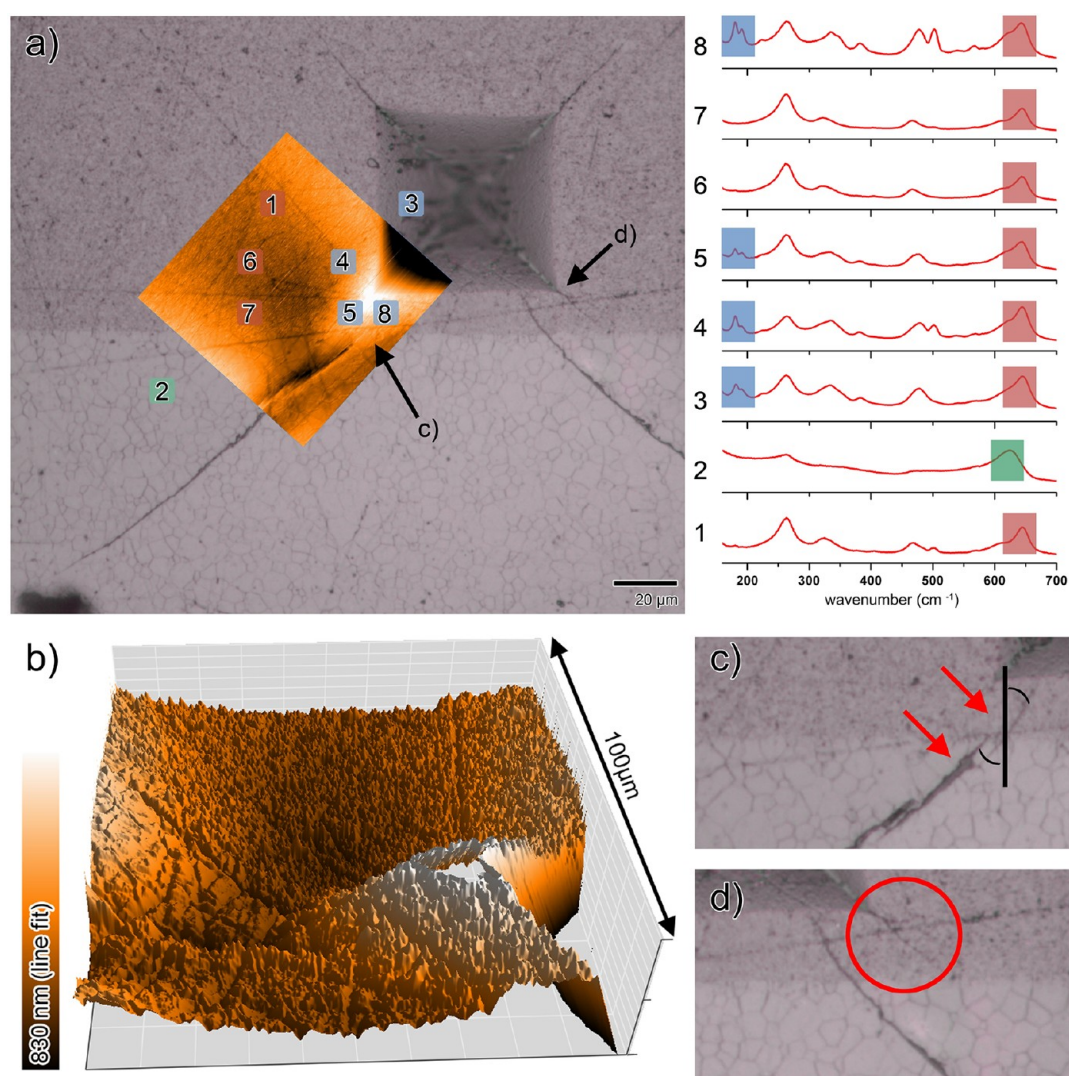


Figure 6. Optical micrographs showing (a) overview of an indent performed on one TZ-3Y layer with superimposed AFM and Raman spectroscopical data, (b) 3D AFM topography corresponding to panel a, and (c) crack propagation (red arrows) and (d) stopping (red circle) through the interface with the TZ-8Y layer.

clearly go through the corners of the indent. It is worth mentioning the existence of scratches in the surface. The possible influence of these scratches in the crack development and propagation will be taken into account in the following discussion. However, these scratches are not deep defects but rather superficial.

The SEM inspection of the fractured surface of a multilayered specimen subjected to 4-PBT revealed significant crack deflection present on the interface between the TZ-3Y and TZ-8Y layers (red circles in Figure 7).

DISCUSSION

EPD was used to produce zirconia multilayered specimens with alternating layers of TZ-3Y and TZ-8Y with decreasing thickness. Samples were consolidated at sintering temperatures of 1450 °C (Figure 3a).

The layers thickness (Figure 3) of the multilayered specimens obtained had a dependency with both the zirconia powder concentration present on the used suspensions and the whole deposition time or “order” of layers. Indeed, the big decrease in the first TZ-3Y layer between samples subsequently produced from one TZ-3Y suspension reveals the direct

dependency of the layer thickness with the amount of TZ-3Y powder present in the suspension. Moreover, although not so significant, the same decreasing tendency can be generally seen for all layers (both TZ-3Y and TZ-8Y) when comparing the second and third replicates (red and blue lines in Figure 3b, respectively). However, it is worth mentioning the smaller thickness of the second layer (TZ-8Y) in the first replicate compared with the second and third replicates. A possible explanation for this difference could be the effect of the shielding on the electrical field between the electrodes produced by the first layer (TZ-3Y), which is significantly thicker for the first replicate. This shielding effect would also explain the decrease in the layers thickness with its order of appearance. Theoretically, this decrease in the electrical field due to the shielding of previous layers should be exponential when layering TZ-3Y and TZ-8Y layers separately.¹⁴ Indeed, for the TZ-3Y layer, this exponential decrease can be seen in the three replicates. However, this exponential decrease is not so clear for the TZ-8Y layers, where we can only observe it in the third replicate. This result may be due to the interrelation of the TZ-3Y and the TZ-8Y deposition process and the shielding

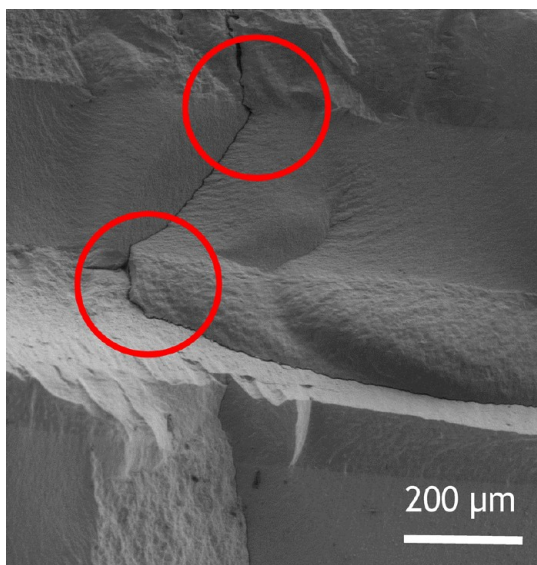


Figure 7. SEM micrograph of the fractured surface of a multilayered specimen subjected to a four-point bending test. Red circles point out significant crack deflections in the layers interface.

between the two different layers, which also have a different ionic conductivity.

EDX analysis (Figure 5) confirmed a change in the corresponding yttrium, zirconium, and oxygen amounts of the respective cubic and tetragonal layers. However, it has to be mentioned that the yttrium atoms have been proved to tend to enrich the cubic grains in front of the tetragonal grains.²⁶ It is difficult to say which is the effect of the yttrium atoms distribution on this small scale in the t-c zirconia multilayered specimens as the resolution of the EDX performed is not enough to detect this differences. The yttrium distribution indeed plays a very important role in the final response of the EPD developed t-c zirconia multilayered specimens, as it is the yttrium that rules all of the different phase transformations in the zirconia ceramic. In accordance with the EDX results, the SEM observations (Figure 4) revealed a sharp and well-interconnected interface between two different microstructures between layers. These well-differentiated microstructures between layers were mainly tetragonal (t) and cubic (c). Indeed, this result is in accordance with the $\text{ZrO}_2\text{--Y}_2\text{O}_3$ equilibrium phase diagram, as expected.²⁷ Also, a residual small amount of cubic phase is expected for a 3 mol % Y_2O_3 doping and a temperature of 1450 °C, which was also detected in the form of smaller cubic grains (Figure 4). It is important to notice that for the case of applications where a wet environment is present, as in dental or orthopedic applications, the low-temperature degradation damage related to the yttria doping should be taken into account and further investigated. However, in the case the yttria doping may represent a drawback, another doping, for example, ceria, could be used to stabilize the zirconia cubic and tetragonal phases.^{26,28}

According to the SEM investigations, the interface between the cubic and tetragonal grains layers appears very sharp, although the grain sizes between these two layers are very different, that is, 0.55 μm for the tetragonal grains versus 3.78 μm for the cubic grains. It is important to notice that this interface between these two different grains was created by the EPD of TZ-3Y and TZ-8Y with similar particle sizes. Moreover, the only chemical difference between these two starting

powders is the amount of yttria doping. The difference in the final grain sizes obtained is due to the final phase obtained (tetragonal or cubic), which experiences difference diffusion and grain growth mechanisms.¹ All this should be taken into consideration to understand the crack propagation mechanisms through these t-c multilayered specimens. The t-c zirconia multilayered specimens exhibited several toughening mechanisms that were tested via Vickers indentation and investigated via AFM and Raman spectroscopy. The tetragonal layers showed a short propagation of the developed cracks due to the already mentioned tetragonal-to-monoclinic transformation toughening mechanism. Apart from this expected transformation toughening mechanism, resulting in a topographic increase and indicative Raman shifts, the t-c multilayered specimens also showed several crack deflection and delamination effects at the interface between the tetragonal and cubic microstructures (Figures 6 and 7). Although this preliminary study points out several toughening mechanisms, it is not possible to conclude, whereas the final toughness of the multilayered specimens has been improved compared with a zirconia monolithic specimen. In this sense, according to the initial high toughness of the tetragonal zirconia and the high ionic conductivity of the cubic zirconia, we expect an increase in the toughness in the multilayered specimen when compared with a cubic monolithic specimen and a possible increase in the ionic conductivity compared with a tetragonal monolithic specimen. In this sense, the different properties (both mechanical and electrical) that the multilayered specimens may present depending on the directionality with respect to the layers (perpendicular or parallel to the layers) are also interesting.

More detailed mechanical and conductivity investigations in EPD-processed t-c zirconia multilayered specimens will be addressed in future investigations.

CONCLUSIONS

Tetragonal and cubic zirconia multilayered specimens with a sharp and well-interconnected interface were successfully produced by EPD of zirconia powders with different amounts of doping (3 mol %, TZ-3Y and 8 mol %, TZ-8Y). Thus, EPD was proved to be a suitable technique to obtain ceramic specimens which present different hierarchical levels, that is, layers, microstructures, and dopant amount. This superior microstructural design and composition make these ceramic constructs promising candidates for several applications like SOFCs, TBCs, and biomaterials.

AUTHOR INFORMATION

Corresponding Author

*E-mail: carolina.mochales-palau@charite.de.

Notes

The authors declare no competing financial interest.

ACKNOWLEDGMENTS

The authors thank the “Zentraleinrichtung Elektronenmikroskopie” (ZELMI) for EDX and SEM analysis, as well as Dr. Uwe Kuhlmann (Technische Universität Berlin, Department of Chemistry, Max-Volmer-Laboratory) for supplying the Raman spectra. We gratefully acknowledge the financial support of the DFG (Deutsche Forschungsgemeinschaft) for our project within SPP1420 (<http://spp1420.mpg.de/projects/>)

hierarchy-of-microstructural-features-as-the-origin-of-fracture-resistance-in-dentine-and-ceramic-composites).

■ REFERENCES

- (1) Graeve, O. A. Zirconia. In *Ceramic and Glass Materials*; Schakelford, J. F., Doremus, R. H., Eds.; Springer: New York, 2008; Vol. Chapter 10; pp 169–197.
- (2) Piconi, C.; Maccauro, G. *Biomaterials* **1999**, *20*, 1–25.
- (3) Bocanegra-Bernal, M. H.; De la Torre, S. D. *J. Mater. Sci.* **2002**, *37*, 4947–4971.
- (4) Green, D. J.; Hannink, R. H. J.; Swain, M. V. *Transformation Toughening of Ceramics*; CRC Press: Boca Raton, FL, 1989.
- (5) Lange, F. F. *J. Mater. Sci.* **1982**, *17*, 235–239.
- (6) Lange, F. F. *J. Mater. Sci.* **1982**, *17*, 225–234.
- (7) Goswami, B.; Ray, A. K.; Sahay, S. K. *High Temp. Mater. Processes* **2004**, *23*, 73–92.
- (8) Chen, L. B. *Surf. Rev. Lett.* **2006**, *13*, 535–544.
- (9) Shao, Z. P.; Zhou, W.; Zhu, Z. *Prog. Mater. Sci.* **2012**, *57*, 804–874.
- (10) Roos, E.; Naga, S. M.; Richter, R. N.; Lauf, S.; Awaad, M. *Ceram. Int.* **2012**, *38*, 3317–3326.
- (11) Keyvani, A.; Saremi, M.; Heydarzadeh Sohi, M.; Valefi, Z. *J. Alloys Compd.* **2012**, *541*, 488–494.
- (12) Tiwari, S. K.; Tripathi, M.; Singh, R. *Corros. Sci.* **2012**, *63*, 334–341.
- (13) Chen, Y.; Bunch, J.; Li, T.; Mao, Z.; Chen, F. *J. Power Sources* **2012**, *213*, 93–99.
- (14) Ferrari, B.; Moreno, R. *J. Eur. Ceram. Soc.* **2010**, *30*, 1069–1078.
- (15) Sarkar, P.; Haung, X.; Nicholson, P. S. *Ceram. Eng. Sci. Proc* **1993**, *14*, 707–716.
- (16) Corni, I.; Ryan, M. P.; Boccaccini, A. R. *J. Eur. Ceram. Soc.* **2008**, *28*, 1353–1367.
- (17) Boccaccini, A. R.; Zhitomirsky, I. *Curr. Opin. Solid State Mater. Sci.* **2002**, *6*, 251–260.
- (18) Moritz, K.; Moritz, T. *J. Eur. Ceram. Soc.* **2010**, *30*, 1203–1209.
- (19) Suciu, C.; Tikkanen, H.; Waernhus, I.; Goga, F.; Dorolti, E. *Ceram. Int.* **2012**, *38*, 357–365.
- (20) Ghatee, M.; Shariat, M. H.; Irvine, J. T. S. *Solid State Ionics* **2009**, *180*, 57–62.
- (21) Ghatee, M.; Irvine, J. T. S. *Int. J. Hydrogen Energy* **2010**, *35*, 9427–9433.
- (22) Abramoff, M. D.; Magelhaes, P. J.; Ram, S. J. *Biophotonics Int.* **2004**, *11*, 36–42.
- (23) Zehbe, R.; Goebbels, J.; Ibold, Y.; Gross, U.; Schubert, H. *Acta Biomater.* **2010**, *6*, 2097–2107.
- (24) Drouin, D. *Monte Carlo Simulation of Electron Trajectory in Solids*, Version 2.42; University of Sherbrooke, 2002.
- (25) Phillippi, C. M.; Mazdiyasn, K. S. *J. Am. Ceram. Soc.* **1971**, *54*, 254–258.
- (26) Chevalier, J.; Deville, S.; Münch, E.; Jullian, R.; Lair, F. *Biomaterials* **2004**, *25*, 5539–5545.
- (27) Scott, H. G. *J. Mater. Sci.* **1975**, *10*, 1527–1535.
- (28) Chevalier, J. *Biomaterials* **2006**, *27*, 535–543.